Electronic Supplementary Material (ESI) for ChemComm.

Supporting Information:

Structure, transport and photoconductance of PbS quantum dot monolayers functionalized with a Copper Phthalocyanine derivative

A. André[a], C. Theurer[a], J. Lauth[b], S. Maiti[c], M. Hodas[c], M. Samadi Khoshkhoo[a], S. Kinge[d], A. J. Meixner[a,e], F. Schreiber[c,e], L. D.A. Siebbeles[b], K. Braun[a], M. Scheele[a,e]

[a] Institute of Physical and Theoretical Chemistry, University of Tübingen, Auf der Morgenstelle 18, 72076 Tübingen, Germany.

[b] Chemical Engineering Department, Delft University of Technology, Van der Maasweg 9, 2619 HZ Delft, The Netherlands.

[c] Institute of Applied Physics, University of Tübingen, Auf der Morgenstelle 10, 72076 Tübingen, Germany.

[d] Toyota Motor Europe, Materials Research & Development, Hoge Wei 33, B-1930, Zaventem, Belgium.

[e] Center for Light-Matter Interaction, Sensors & Analytics LISA+, University of Tübingen, Auf der Morgenstelle 15, 72076 Tübingen, Germany.

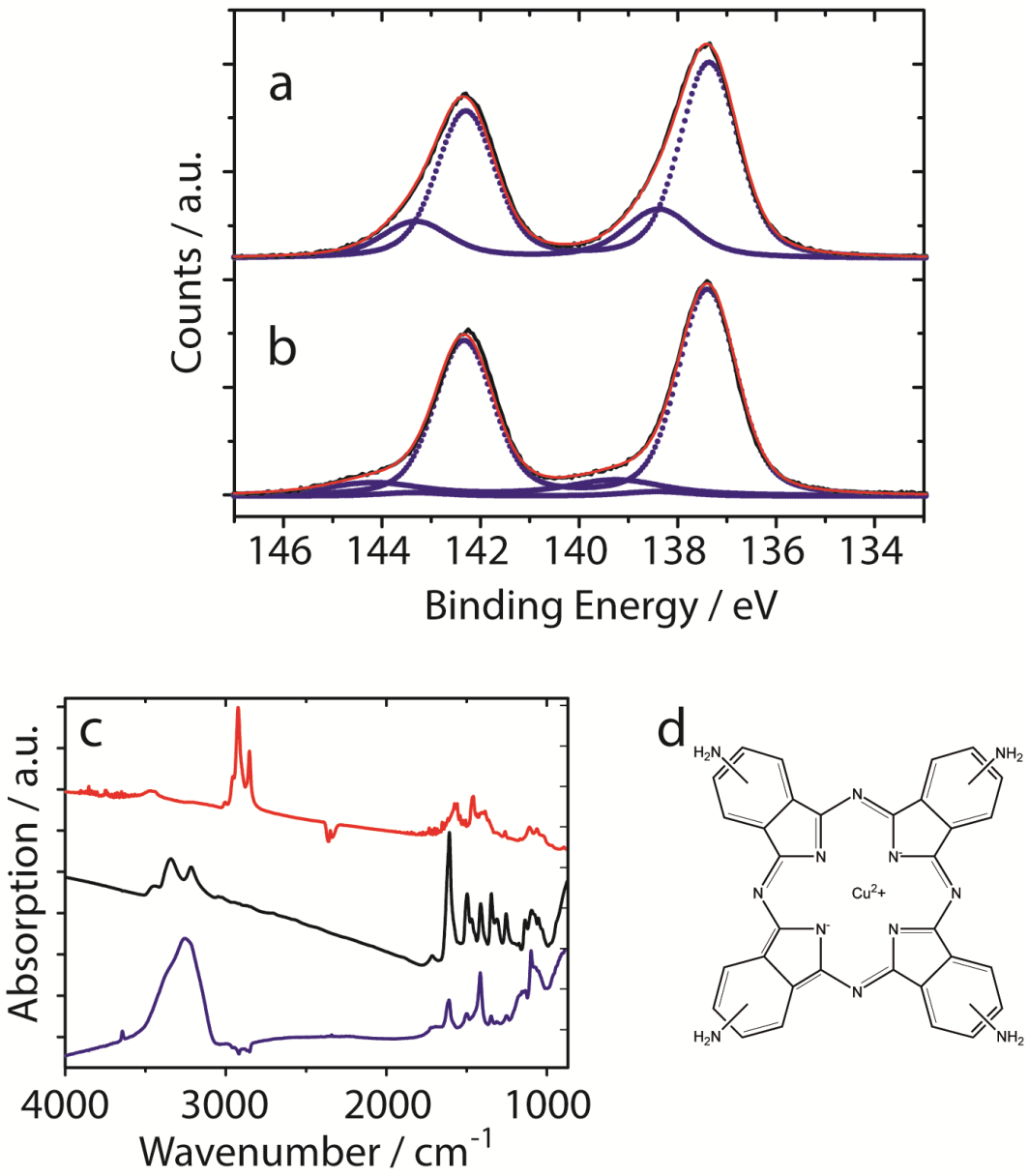

Figure S1. *XPS spectra of the Pb 4f region of* ***a)*** *PbS NCs functionalized with Pb[Oleate]*$_2$ *and* ***b)*** *PbS NCs after ligand exchange with Cu-4APc.* ***c)*** *FT-IR spectra of the same compounds ("1" with oleate capping and "3" with Cu-4APC, respectively) including pure Cu-4APc (2).* ***d)*** *Structural formula of Cu-4APc.*

XPS measurements in the Pb-4$f_{5/2}$ and Pb-4$f_{7/2}$ spectral region of the same PbS NC sample before (**Fig. S1a**) and after exchange with CuTAPc (**Fig. S1b**) reveal the occurrence of two Pb species before and three Pb species after ligand exchange. The

strong signals at 142.7 eV and 137.8 eV for Pb-$4f_{5/2}$ and Pb-$4f_{7/2}$,respectively, are consistent with bulk PbS from the interior of the NCs. The weaker signals at 143.8 eV and 138.8 eV can be assigned to surface Pb bound to oleic acid/oleate. After ligand exchange, the latter signal is significantly reduced and a new species at 144.8 eV and 139.8 eV appears, which we attribute to surface Pb, bound to Cu-4APc. Moreover, a nitrogen signal appeared in the N-1s spectral region after ligand exchange.

FT-IR results (**Fig. S1c**) show good agreement between the spectrum of Cu-4APc functionalized NCs and the spectrum of pristine Cu-4APc. For the pure molecule (see **Fig. S1d** for the chemical structure), most notable IR bands are in good agreement with literature for non-functionalized Cu-phthalocyanine. We additionally find the N-H-vibrations at 3444, 3342 and 3216 cm^{-1}. For the Cu-4APc functionalized PbS NC sample after ligand exchange, we observe the strong bands at 1608 cm^{-1} (ν(C-C) stretch in pyrrol), 1496 cm^{-1} (β(C-H) aryl), 1412 cm^{-1} (ν(C-H) in plane), 1348 cm^{-1} (ν(C-C) in isoindole), 1253 cm^{-1} (ν(C-N) in isoindole) as well as at 1096 cm^{-1} (β(C-H) in plane deformation). Most of these bands are slightly shifted with respect to the corresponding bands in the pure molecule. This is often observed for surface-bound molecules. The amino group vibrations are heavily broadened, which points toward their role as bonding groups. The remaining vibrations are probably not visible due to either lower signal intensity or damping due to spatial constraints in the COINS.

Synthetic procedures.

Cu 4,4‘,4‘‘,4‘‘‘-Tetraaminophthalocyanine (Cu-4APc) was synthesized in two steps following Jung et al., and oleic acid-capped PbS QDs were obtained according to Weidman et al.[1][2]All materials were processed and characterized under inert conditions in a glovebox.

Particle size distribution was investigated with the help of TEM images. The diameter of a set of about 500 particles was measured. The sizing curve is shown in **Fig. S2**. Absorption data was measured in order to estimate the size distribution of a batch of smaller particles (**Fig. S2**).

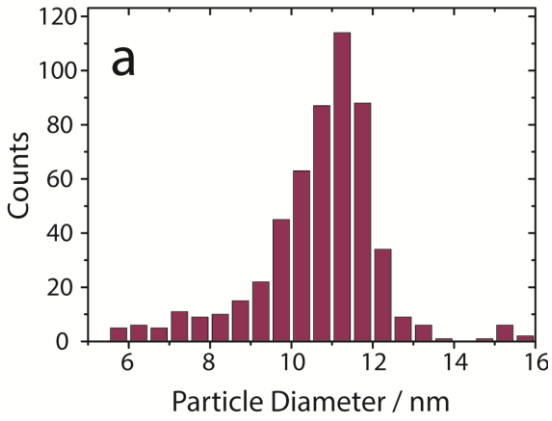

Figure S2. *Size histogram of the PbS particles used in this work. On the assumption of a fully cubic shape, the average edge length is (10.7 ± 1.5) nm.*

Ligand exchange at the liquid-air interface.

The substrate to be coated was put onto a slanted substrate holder in the a home-made, sealable reaction chamber filled with 8 ml acetonitrile (**Fig. S3**). The inclined sample position greatly improves the drying procedure of the deposited film. After sealing the chamber, 80 µl of a PbS nanocrystal solution in a 2:1 mixture of octane and hexane were deposited on top of the acetonitrile. The particle deposition rate is one of the most critical parameters and was therefore controlled by using a syringe pump. Low rates around 0.2 ml/min yielded uniform monolayered thin-films, while higher rates (i.e. 1.0 ml/min) yielded thicker and rougher films. The nanoparticle concentration (typically around 3 µM as determined spectroscopically)[3] was chosen so as to have enough particles to completely cover the acetonitrile surface.

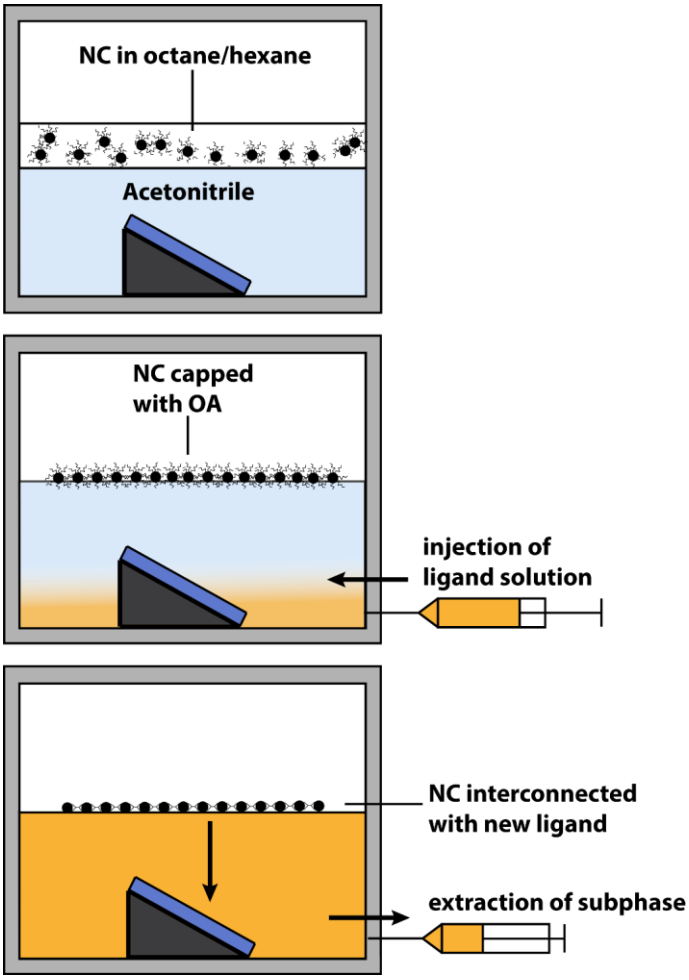

Figure S3. *Basic scheme of the thin film preparation procedure in the closed reaction chamber.*

The octane/hexane completely evaporated within ~2 min and the nanoparticles formed a thin film floating on top of the acetonitrile phase. 200 µl of a solution of 1mg/ml Cu4APc in dimethylsulfoxide (DMSO) were carefully injected into the sub-phase and the ligand was allowed to diffuse over the duration of 2 hours. We carefully removed the now homogeneously coloured solution to deposit the nanocrystal film on top of the substrate. The substrate was slowly dried, washed with DMSO to remove excess ligand, baked out at 100°C for 1min and kept under vacuum overnight.

Characterization techniques.

FT-IR spectroscopy.

FT-IR spectroscopy was performed with a Vertex70 and IFS48 FT-IR Spectrometer (Bruker). Nanoparticle samples were exchange and deposited onto polished CaF_2 windows as described under "Ligand exchange at the liquid-air interface". In order to increase the signal-to-noise ratio, two nanocrystal thin films were deposited on top of each other. Reference spectra were measured on a sample of drop-cast Cu-TAPc and a double layer of the pristine PbS nanocrystals.

X-ray photoemission spectroscopy (XPS).

XPS measurements were carried out using a SPECS spectrometer equipped with an XR50 X-ray source (Al Kα, working at 12.5 kV and 20 mA, 1486.61 eV) and a PHOIBOS 100 MCD analyzer. Samples were prepared as described under "Ligand Exchange". The pressure in the analyzer chamber was maintained below 3×10^{-10} mbar during the measurements. No changes in the core level signals of the as-prepared films and the films under X-ray irradiation were observed, underlining the stability of the molecules during data acquisition. The resolution in XPS measurements is determined as 0.8 eV (calculated from the width of Fermi edge on the Au substrate). The binding energies were corrected for electrical charge effects by referencing to the Au 4f peak, which was assumed to have a binding energy of 84.0 eV. The photoelectrons were detected at a takeoff angle of $\Phi = 0°$ with respect to the surface normal. Data were converted to VAMAS format and processed using Unifit2014 software. Data fitting was performed using Gauss-Lorentz profiles. The background was calculated and subtracted using the Shirley method. Each spectrum was also corrected for satellite peaks ($\Delta = 9.8$ and 11.8 eV from $K_{\alpha 3}$ and $K_{\alpha 4}$, respectively).

Small-angle X-ray scattering (GISAXS, XRR, GIWAXS).

Grazing angle small angle and wide angle x-ray scattering (GISAXS, GIWAXS) and reflectivity measurements were performed on commercially available tabletop systems. GISAXS and GIWAXS measurements were performed at a small angle X-ray diffractometer, Xeuss 2.0 laboratory beamline from Xenocs, France, with a fine focus source of wavelength 1.5419 Å (CuK_α). An incident beam of size 0.5 x 0.5 (V x H) mm^2 was used with a grazing incidence of 0.2º which is below the critical angle of the Si-substrate. A 2D 300K-Pilatus detector was employed at a distance of 2.5 m from the sample center to collect GISAXS data and another kept at a distance of 0.158 m with an off-set of 36 degree to cover a wide range of momentum wave-vector transfer (q) values. Each sample was measured for 1 hour to improve statistics. To improve the statistics of the line profiles, the ROI (red dotted box in the main body of the manuscript) was integrated along the q_z direction. The average domain size of the superlattices was extracted by Lorentzian fitting of the background-subtracted correlation peak at q_y = 0.0475 $Å^{-1}$ (**Fig. 2b**). Fitting of the second correlation peak is shown in **Fig. S4**. GISAXS and GIWAXS scans were taken at the same angle of incidence at 0.2 °.

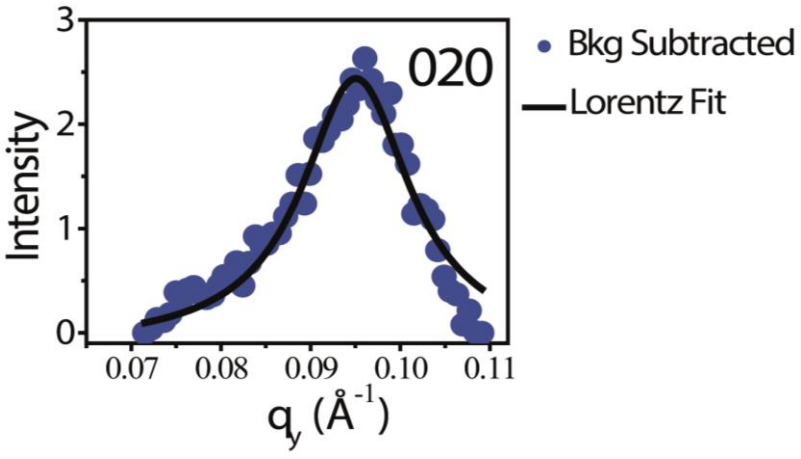

Figure S4 *Lorentzian fit of the second background-subtracted correlation peak at* q_y*=0.095* $Å^{-1}$.

The XRR data and the corresponding electron density profile in **Fig. S5** obtained by fitting are in good agreement with a single layer of Cu-4APc functionalized PbS NC film (e.g. the average height of the film extracted from XRR is ~13 nm.)

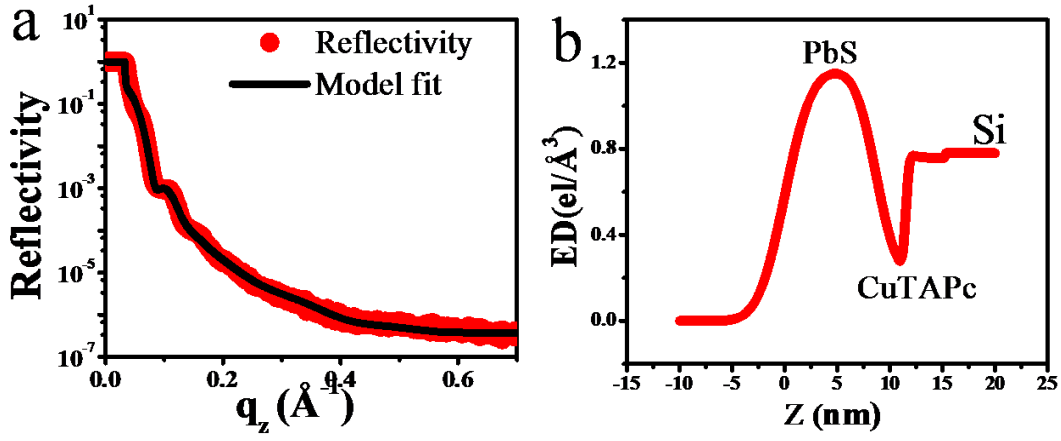

***Figure S5**. **a**) XRR profile of a typical PbS-Cu4APc film and it's fit. **b**) Electron density profile of the film along depth of the film (z), obtained from the XRR fitting.*

Field-effect transistor (FET) measurements.

Electrical measurements were conducted using a Keithley 2634B dual source-meter unit, controlled by the included test script builder program. Substrates were contacted using a home-built probe station enclosed in a nitrogen glovebox. To ensure operation in the linear regime, a low source-drain bias (VDS = 5V) was employed compared to the gate voltages swept (VGS = 0-40 V), allowing the extraction of linear field-effect mobilities of the injected carriers (μlin) under the gradual-channel approximation,

$$\left.\frac{\partial I_{DS}}{\partial V_{GS}}\right|_{V_{DS}} = \frac{WC_{OX}V_{DS}}{L}\,\mu_{lin} \qquad (1)$$

where W is the channel width, L is the channel length, I_{DS} is the source-drain current, C_{OX} is the capacitance per unit area of the gate oxide. Consistent with previous studies, these PbS quantum dot films exhibit transient decays of current due to trapping of injected carriers. Thus, voltages must be swept quickly (0.1 V ms^{-1}) to minimize the

influence of trapping and ensure repeatable, history-independent measurements. For transfer curves exhibiting a small degree of nonlinearity, the average of the transconductance was used for mobility extraction.

Transmission Line Method (TLM).

The transmission line method allows to determine the parasitic resistances and the sheet resistance of thin films. The principle is based on the change of the total device resistance with varying contact distances. This total device resistance comprises of the materials sheet resistance R_{sheet} and the parasitic resistances R_p, especially due to contact resistance (i .e. injection barriers).

$$R_{on} = R_{sheet} + R_p \quad (2)$$

The TLM method can be used for measurements in the saturation regime or, as in our case, in the linear regime. The advantage of the linear regime is that R_p has a much higher impact on the measured values[4] and can thus be determined with higher accuracy. The specific resistance is measured for devices of different channel lengths. The resulting plot is fitted linearly.[4][5] The fit function's slope yields the contact width dependent sheet resistance $\frac{R_{sheet}}{W}$, while the y-axis intercept yields the total contact resistance R_p. For our measurements we used the same contacts as for the FET set-up and varied between 3 different lengths: 2.5 µm, 10 µm and 20 µm. This allows to extract the contact and sheet resistance of the active layers used for transport properties measurements. The results shown in the main body of the manuscript have been taken on a single substrate with 4 contacts of each size.

THz Conductivity Measurements

The frequency dependent mobility of charge carriers in Cu4APc functionalized PbS NCs was determined by time-domain THz spectroscopy. The laser system used has been described for transient absorption and THz conductivity measurements previously[6]–[8] and data acquisition is briefly discussed here.[6]–[10] PbS NCs functionalized with Cu4APC are excited with 60 fs laser pulses and the conductivity is probed by measuring the change of the amplitude and phase of the THz electric field waveform. This yields the conductivity $\Delta\sigma(\omega, t)$ as a function of the frequency, $f = \omega/2\pi$, of the probing THz field at a varying time *t* after the pump pulse.

A home-built set-up includes the detection of the transmitted THz probe by a single-cycle THz pulse, generated in a $LiNbO_3$ crystal and detected in a ZnTe crystal. A chirped optical pulse used for spectral encoding, allows a single shot detection of the THz waveform. From the measurements we obtain the differential transmission of the THz waveform $\Delta E(t_p, t) = E_{excited}(t_p, t) - E_0(t_p)$ with $E_{excited}(t_p, t)$ the transmitted THz electric field after photoexcitation of the sample and $E_0(t_p)$ the transmitted THz electric field in absence of photoexcitation, t_p is the time between generating and detecting the THz field and t the time delay between the photoexcitation pump pulse and the THz probe pulse. $\Delta E(t_p, t)$ is normalized to E_{max}, the maximum amplitude of the transmitted THz field in absence of pumping. The complex, frequency-dependent conductivity with respect to the THz time delay t_p is then extracted by applying the Fourier transform $F(\omega) = \int_{-\infty}^{\infty} f(t_p) e^{i\omega t_p} dt_p$ and yields:

$$\frac{\Delta E(\omega,t)}{E_0(\omega)} = -\frac{\Delta\sigma(\omega,t)L}{2c\varepsilon_0\sqrt{\varepsilon(\omega)}} \qquad (3)$$

where c is the speed of light, L is the thickness of the sample, ε_0 is the vacuum permittivity, and $\varepsilon(\omega)$ is the dielectric function of the sample. $\sqrt{\varepsilon(\omega)} = n_{eff} = 13.6$ is the effective refractive index of PbS at THz frequencies applied in our evaluation.[11] The real conductivity due to free charges only is given by $\Delta\sigma = e(n_e\mu_e + n_h\mu_h)$ with e the elementary charge, μ_e (μ_h) the mobility of electrons (holes) and $n_e(n_h)$ the average density of electrons (holes). For an absorbed photoexcitation density per unit area $N_a = I_0F_A$ (I_0 is the pump laser fluence, F_A is the fraction of photons absorbed), $n_{e,h} = \Phi_{e,h}(t)N_a/L$, we can determine the sum of the product of the photogeneration charge carrier quantum yield and the electron and hole mobility as:

$$\phi_e(t)\mu_e + \phi_h(t)\mu_h = -\frac{\Delta E(\omega,t)}{E_0(\omega)}\frac{2c\varepsilon_0 n_{eff}}{eN_a} \qquad (4)$$

Note that equation (4) does not require the actual sample thickness L, but only the photoexcitation density N_a per unit area.

Characterization of the Light Effect Transistor

The photocurrent measurements were performed on a homebuilt inverted confocal microscope (**Fig. S6**). As a primary excitation source we used a linearly polarized 633 nm He-Ne laser. The radial/azimuthal polarized doughnut mode (RPDM/APDM) was generated by means of a mode converter (MC). The MC consists of a 4 quadrant λ/2 retardation plate that locally rotates the linear polarization of the incoming beam. By rotating the mode converter MC by 90° one can turn a APDM into an RPDM and vice versa. After the MC, a spatial filter consisting of two lenses (L1/2) and a pinhole (PH) is used to reduce beam distortions arising from structural defects of the MC. The spatially filtered RPDM/APDM is directed to the objective lens (O) by a 50:50 non-polarizing beamsplitter (BS 1). For excitation and detection, we used an oil immersion objective lens with a numerical aperture (NA) of 1.25.

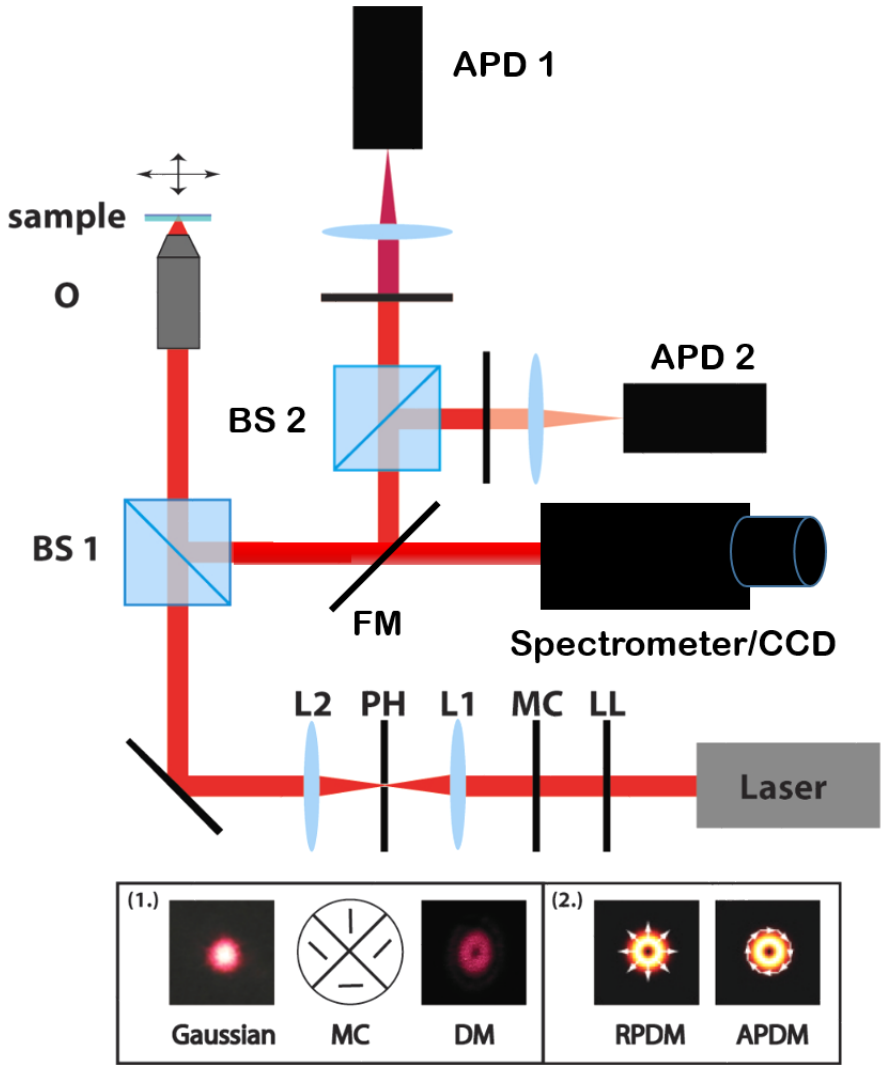

Figure S6 *Scheme of the used confocal optical microscope. The linear polarized light of the laser is transformed into higher oder laser modes via a mode conversion consisting of a mode converter (MC) and spatially filtered with pinhole (PH) in the focus of a telescope (L1 and L2). For the photocurrentmeasurements the APDM is used.*

Images were acquired by raster scanning the sample, and signals were collected by a spectrometer with an attached cooled CCD detector or via a flipping mirror (FM) by two Avalanche photo diodes (APD 1/2). The 50:50 non-polarizing beamsplitter (BS 2) splits the signal equally on both APDs. Before reaching APD 1, a band pass filter (BP) centered at λ=633 nm permits to detect only the elastically scattered light. In front of

APD 2, a 633 nm long pass filter (LP) was placed. This detector was used to collect the luminescence signal. Thus, our setup is capable to simultaneously detect the luminescence and the elastically scattered light. In addition, the current across the channel was measured in relation to the position of the laser beam to construct a "current image". This image is obtained by raster scanning the sample analogously to the luminescence image, but using the current measured across the channel for a given focus position as the contrast information. E.g. a bright spot in **Fig. 4b** means that optical excitation of this sample location invokes a relatively large current flow across the channel. This way, we obtain simultaneous "light images" and "current images".

For the LET measurements we used glass substrates, on which gold contacts were deposited by vacuum deposition. A channel with approximately 250 nm length and 100 µm was cut by a focused ion beam in these contacts. The total size of the contacts is 500x 500 µm (see **Fig. S7**). PbS-Cu4APc was deposited onto the substrate to cover the channel as described under "Ligand exchange at the liquid-air interface".

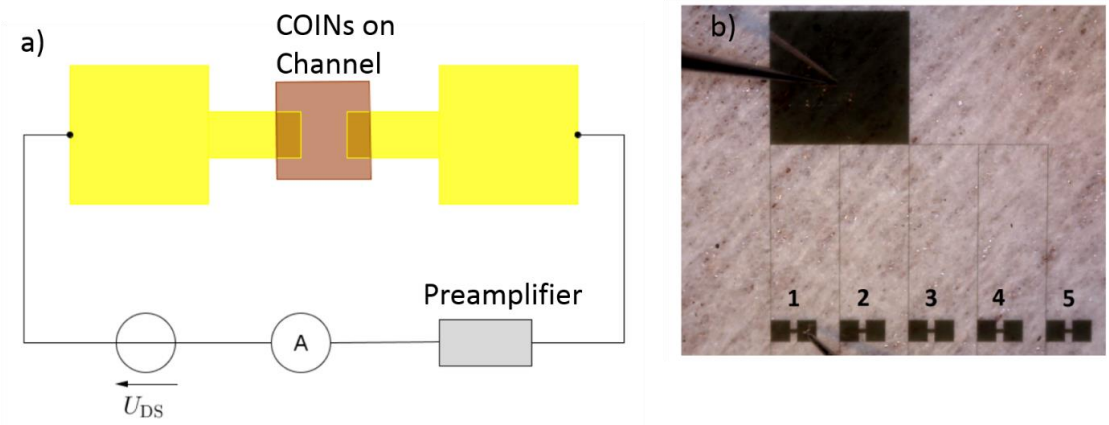

Figure S7*. Simplified sketch of the light effect transistor (a) and the measurement circuit parallel to the optical experiments. (b) Glass substrate with 5 gold electrodes.*

In these measurements, only a small area of the channel (see **Fig. S8** zoom in) is illuminated and film inhomogeneities, such as voids or poor local contact to the Au electrodes, can strongly affect the current image. An example of a typical density of voids can be deduced from the elastic-scattered light image in **Fig. S8**, where the contrast scales with the amount of PbS-Cu4APc coverage. A region without any nanocrystals can be seen in the up right corner (red box).

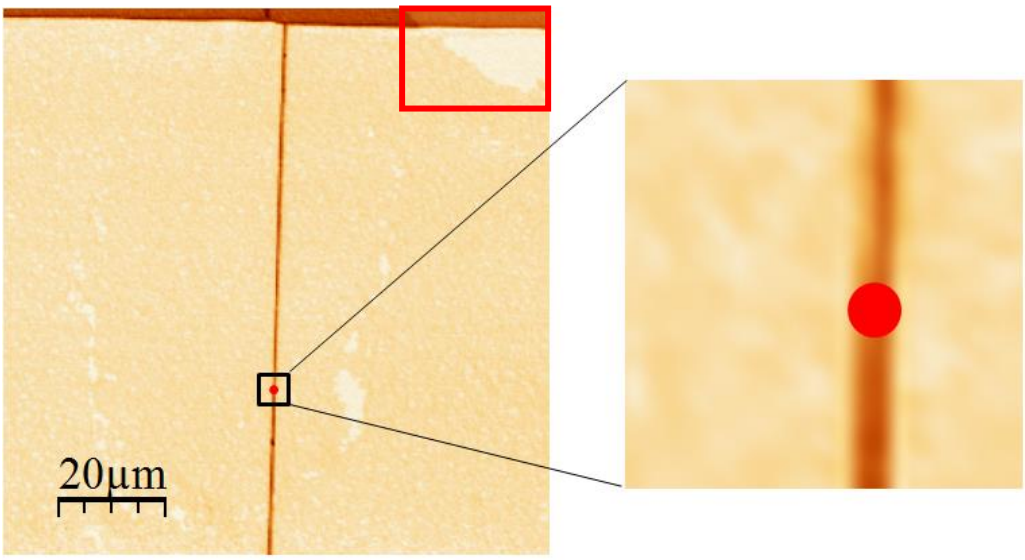

Figure S8 *Elastic scattering image of the LET channel. A slight contrast appears due to the coverage of COINs. The red dot illustrates the size of the laser focus in relation to the size of the LET device. As indicated in the inset, the channel is much smaller than the focus and therefore the collected image is a convolution of the channel width as well as the focus and dominated by the size of the focus.*

In addition, the small laser focus invokes a relatively small increase in the conductivity of the film since new carriers are only generated in the illuminated area, while it remains constant in the dark areas. This means that the increase of the conductivity due to illumination is much larger than the increase of the current suggest. To alleviate all of the above issues, we first determine the mean current under illumination (**Fig. S9 a**) by

averaging point by point along the channel and compare it to the mean current without illumination (I_{off}) (**Fig. S9 b**). This smoothes the effect of inhomogeneities.

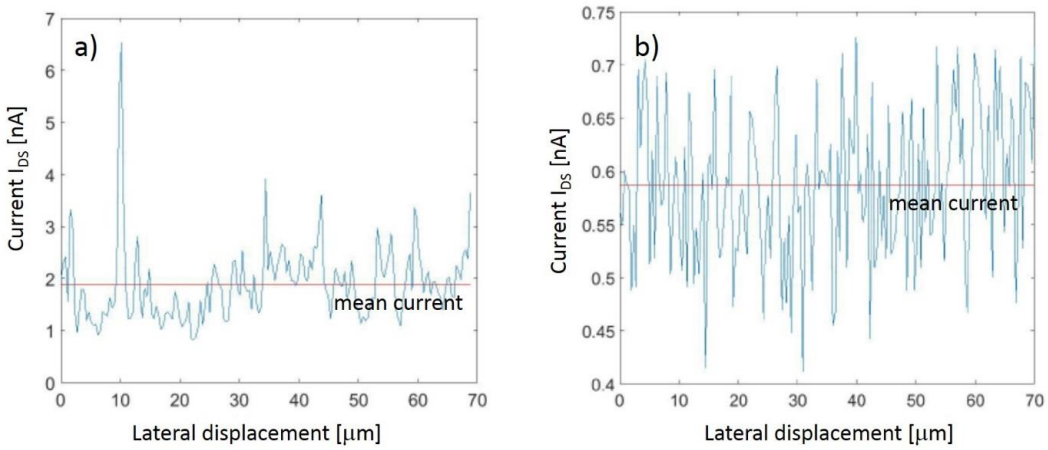

Figure S9. *Calculation of the mean currents on the illuminated channel (a) and on the gold electrodes (b)*

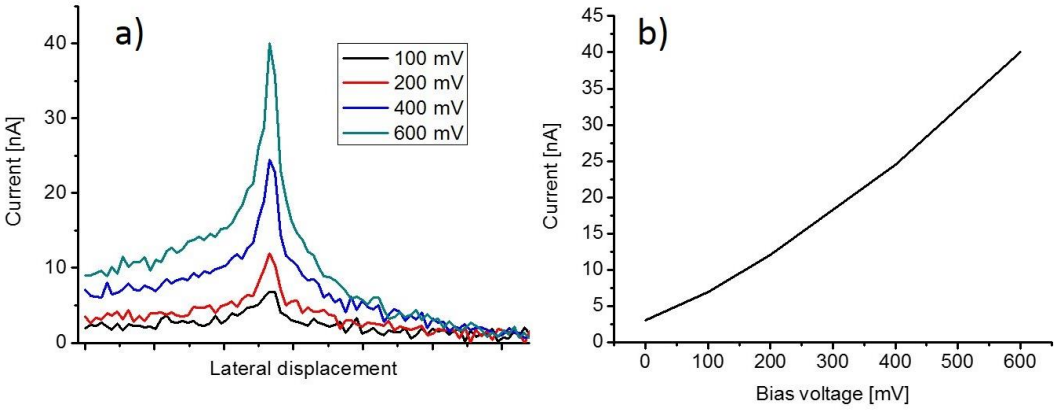

Figure S10*. (a) Line scans over a channel at the same local area with different bias voltages. The currents are increasing with increasing bias voltage linearly (b), indicating ohmic behavior.*

The mean illuminated current is then multiplied by a factor of 200 to obtain the integrated illuminated current (I_{on}). We take a factor of 200, because the area of illumination (with maximal intensity) is approximately 500 nm wide and the channel has a total width of 100 µm, e.g. roughly 200 times larger than the focus. This integrated

current represents a more appropriated measure for the photosensitivity of the complete device. Both plots, the mean and integrated currents, are displayed in **Fig. 4d**.

References.

[1] S.-H. Jung, J.-H. Choi, S.-M. Yang, W.-J. Cho, C.-S. Ha, *Mater. Sci. Eng. B* 2001, **85**, 160.

[2] M.C. Weidman, M.E. Beck, R.S. Hoffman, F. Prins, W.A. Tisdale, *ACS Nano* 2014, **8**, 6363.

[3] I. Moreels, K. Lambert, D. Smeets, D. De Muynck, T. Nollet, J.C. Martins, F. Vanhaecke, A. Vantomme, C. Delerue, G. Allan, Z. Hens, *ACS Nano* 2009, **3**, 3023.

[4] J. Zaumseil, K.W. Baldwin, J.A. Rogers, *J. Appl. Phys.* 2003, **93**, 6117.

[5] S. Luan, G.W. Neudeck, *J. Appl. Phys.* 1992, **72**, 766.

[6] W.H. Evers, J.M. Schins, M. Aerts, A. Kulkarni, P. Capiod, M. Berthe, B. Grandidier, C. Delerue, H.S.J. van der Zant, C. van Overbeek, J.L. Peters, D. Vanmaekelbergh, L.D.A. Siebbeles, *Nat.Commun.* 2015, **6**, 8195.

[7] L.T. Kunneman, J.M. Schins, S. Pedetti, H. Heuclin, F.C. Grozema, A.J. Houtepen, B. Dubertret, L.D.A. Siebbeles, *Nano Lett.* 2014, **14**, 7039.

[8] L.T. Kunneman, M. Zanella, L. Manna, L.D.A. Siebbeles, J.M. Schins, *J.Phys.Chem.C* 2013, **117**, 3146.

[9] J.E. Murphy, M.C. Beard, A.J. Nozik, *J.Phys.Chem.B* 2006, **110**, 25455.

[10] R. Ulbricht, E. Hendry, J. Shan, T.F. Heinz, M. Bonn, *Rev.Mod.Phys.* 2011, **83**, 543.

[11] G. Guizetti, A. Borghesi, in (Ed: E.D. Palik), *Handbook of Optical Constants of Solids*. Lead Sulfide (PbS). Elsevier: New York **1998**.